The Electrical Properties of Pure and Doped Nanocrystalline Cerium Oxide

by

Erin Baker Lavik

S.B., Materials Science and Engineering (1995)
Massachusetts Institute of Technology

Submitted to the Department of Materials
Science and Engineering in Partial
Fulfillment of the Requirements for the Degree of

Master's of Science

at the

Massachusetts Institute of Technology

June 1997

© 1997 Massachusetts Institute of Technology
All rights reserved

Signature of Author..
Department of Materials Science and Engineering
May 9, 1997

Certified by..
Professor Yet Ming Chiang
Kyocera Professor of Ceramics
Thesis Supervisor

Accepted by..
Professor Linn W. Hobbs
John F. Elliott Professor of Materials
Chairman, Departmental Committee on Graduate Students

The Electrical Properties of Pure and Doped
Nanocrystalline Cerium Oxide

by

Erin Baker Lavik

Submitted to the Department of Materials Science and
Engineering on May 9, 1997 in partial fulfillment of the
requirements for the Degree of Master of Science in
Materials Science and Engineering

ABSTRACT

Nanocrystalline cerium oxide is an attractive material for catalysis of environmentally hazardous gas-phase species such as sulfur dioxide and carbon monoxide. Oxygen vacancies in cerium oxide are believed to coordinate and aid in the transfer of oxygen ions between the reactive species. We have sought to characterize these defects in nanocrystalline cerium oxide as a function of the heat treatment and grain size of the material. By understanding the fundamental defect thermodynamics of the nanocrystalline material, we have determined the unique behavior of this material which appears to contribute to its role as a catalyst. This has been achieved through the formation of dense (>90% theoretical density) nanocrystalline pellets which were studied via impedance spectroscopy to separate the contributions of the grain boundary and bulk material. This work shows that nanocrystalline cerium oxide exhibits enhanced electrical conductivity and reduced behavior in regimes where the conventional material is not reduced, and we attribute this to the presence of low-energy sites for defect formation at the grain boundaries. It has also been found that annealing the material at moderate temperatures for short times without coarsening leads to an atomic relaxation process which eliminates these low energy sites for reduction. Doped nanocrystalline cerium oxide has also been studied to explore the interaction between the unique character of the nanocrystalline material and the effects of doping on the conductivity.

Thesis Supervisor: Professor Yet-Ming Chiang
Title: Kyocera Professor of Ceramics

Table of Contents

List of Illustrations and Figures

List of Tables

Acknowledgments

I have now been at M.I.T. for almost six years. I have really enjoyed in great part because I have been surrounded by incredible people. First, there is my advisor, Professor Chiang. He is a brilliant scientist who is both creative and insightful. It has been a constant honor to work with him. Very few other people could be so patient with a student who thinks that they want to leave their field and pursue an entirely new one. Even fewer could be so supportive of such a change. Professor Chiang has given me a great deal, but most of all he has given me that support. When I have struggled, he has been their to encourage me and to help me in every way he can. When others have believed that I should not continue, he has fought so that I could have the chance to prove myself. In exchange, I can only offer my deepest thanks and respect.

So far, I've found that while graduate school can be a wonderful place, it will, at some point, really stink. I am thankful to all of those people in my group who helped me with my research and made me laugh when it failed. Jian Luo, Jonq-Ren Lee, Douglas Blom, Harold Ackler, Haifeng Wang, and Leszek Hozer all contributed to this work. They also provided the enormously funny, and often witty conversation that made the lab a bearable place when it seemed like we would never leave.

I am also grateful to all of the people outside of my group who helped me with this work, in particular, Thomas Chen and Ofer Porat. Thomas taught me how to run the sputtering machine, and Ofer helped me learn to make impedance measurements.

I would also like to thank some of the wonderful friends I have made here. I am grateful to Arun Seraphin, Erika Abbas, Eric Werwa, Tracey Burr, and the kids, Aaron Blanchet, Debra Lightly, and Mike Groenert, for listening to my stories, teaching me the "code", and making me laugh instead of throw in the towel.

I am grateful to my officemates, particularly Srikar. He is hysterically funny, helpful, and a good friend. I also have to thank Jon Hester for his humor and unerring sense of the absurd. I would have never made it through the orals without him.

I would also like to thank Professor Kolenbrander for his patience and compassion. I have learned a great deal from him. He has been one of the best teachers I have had at M.I.T., and I feel honored to call him a friend.

I would also like to thank Ranjini Srikantiah for being one of the best friends a person could ever have and for proofreading this document.

Mom and Dad, Thank you. I do not know the words to acknowledge all you have given me other than to say that you are my strength and inspiration. Tak.

1. Introduction

Cerium oxide is an important catalytic material for the oxidation and reduction of gas phase species such as carbon monoxide and sulfur dioxide[1,2]. Nanocrystalline cerium oxide exhibits significantly improved catalytic properties, including the ability to achieve greater conversion at lower temperatures than its coarse-grained counterpart for the aforementioned reactions[3]. Surface oxygen defects are believed play an essential role in the redox process by coordinating with the gas molecules to facilitate the transfer of oxygen ions from SO_2 to CO.

Thus, the oxygen vacancies, the primary ionic defects in undoped cerium oxide, play a critical role in low temperature, environmentally friendly catalysis. Characterization of these defects is critical to the understanding and exploitation of cerium oxide as a catalyst. Hence, we have studied these defects through an analysis of the electrical properties of cerium oxide as a function of grain size.

Cerium oxide, in its doped form, is also a candidate for solid oxide fuel cells. Typically, CeO_2, which is in the fluorite structure, is doped with a trivalent cation, such as gadolinium. The gadolinium 3+ substitutes on the cerium 4+ sites, leading to the formation of compensating oxygen vacancies ($V_O^{\cdot\cdot}$) by the following defect reaction:

$$Gd_2O_3 \xrightarrow{CeO_2} 2Gd_{Ce}' + V_O^{\cdot\cdot} + 3O_O^X \qquad \text{Eq. 1}$$
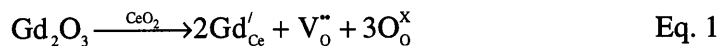
The high concentration of oxygen vacancies coupled with the location of the oxygen atoms in the tetrahedral positions makes doped cerium oxide a good oxygen conductor. Cerium oxide can also be a mixed conductor, conducting both electrons and oxygen vacancies, over certain temperature and oxygen partial pressure regimes when it is lightly doped.

There are a number of applications for cerium oxide, but there are also purely scientific reasons for this work that cross the boundaries of a specific ceramic material and address basic properties of nanocrystalline materials. There is limited information regarding the size-dependence of properties at fine grain-sizes. This work ultimately seeks to determine whether the properties of nanocrystalline materials are unique or simply size-scaled effects. Cerium oxide is ideal for such work because nanocrystalline size scales are easily attained and the electrical properties of the single crystal material have been well characterized.

2. Background

2.1 Applications for Nanocrystalline Cerium Oxide

2.1.1 Catalysis

Ceria is used as a support material in automotive three-way catalysts as well as in industrial applications. Three way catalysts are designed to simultaneously catalyze reactions involving CO, hydrocarbons, and NO_x to eliminate these species from the exhaust[4]. The typical catalyst contains a precious metal such as platinum, palladium, or ruthenium, and a support. The support is generally an oxide such as ceria, alumina, nickel oxide, or some combination of the above. Several authors have found that the support plays an important role in the catalytic behavior. Yao and Yao[5] showed that cerium oxide acted as an oxygen storage material, meaning that it could undergo "rapid change in oxidation state upon a change in the redox potential of the exhaust gas". They also found that this oxygen storage capacity was influenced by the calcination temperature of the cerium oxide; it decreased significantly when the oxide was calcined at 800 °C rather than 600 °C. Fine powders were used in this work.

Su et al.[6] have shown that there is a synergistic effect between the ceria and the precious metal. The precious metal is believed to aid in the redox behavior, thus, improving the oxygen storage capacity of the catalyst. However, it is apparent that more occurs than a simple interaction between the metal and oxide. Hardacre et al.[7] studied the catalytic behavior of ceria on (111) platinum wafers and found that the most active surfaces were those in which the cerium oxide completely covered the platinum wafer and existed in a disordered state. They further saw that the activity dropped significantly upon annealing the material at temperatures above 900 K, and they attributed this behavior to the removal of "open crystal planes at which oxygen vacancy creation is favored". However, they made no direct measurements of the defects.

From the above work, it appears that the catalytic properties of fine-grained cerium oxide change upon heating the material above approximately 700 °C. What is not clear from the above is how the material changes: whether the defect formation energies stay the same but the density of sites decreases with increasing grain size or whether the defect formation energies actually change with heat treatment. Thus, the present work explores the effect of heat treatment on the defect behavior through a study of the conductivity of ceria.

Obviously, catalysis occurs on free surfaces whereas the electrical experiments employed in this work explore the nature of defects at the grain boundaries. However, it is

likely that defect formation at the free surfaces is correlated with defect formation at the grain boundaries.

2.1.2 Solid Oxide Fuel Cells (SOFC's)

Steele[8,9] provides a substantial examination of the theory and application of SOFC's. SOFC's rely on an oxygen partial pressure gradient to drive oxygen ions through the electrolyte, and simultaneously drive the current, a result of the electroneutrality condition, across the load (figure 1). SOFC's consist of two primary components: the electrolyte and the electrodes. The electrolyte must exhibit high ionic conductivity at moderate temperatures to achieve the necessary powder densities to make SOFC's competitive. Materials of the fluorite structure readily lend themselves to this task due to the location of the oxygen atoms in adjacent tetrahedral positions. While pure cerium oxide is an electronic semiconductor, cerium oxide doped with trivalent cations such as gadolinium, exhibits substantial ionic conductivity. Cerium oxide doped with 23% gadolinium exhibits an ionic transference number greater than 0.95 for temperatures above 600 $^\circ$C[10].
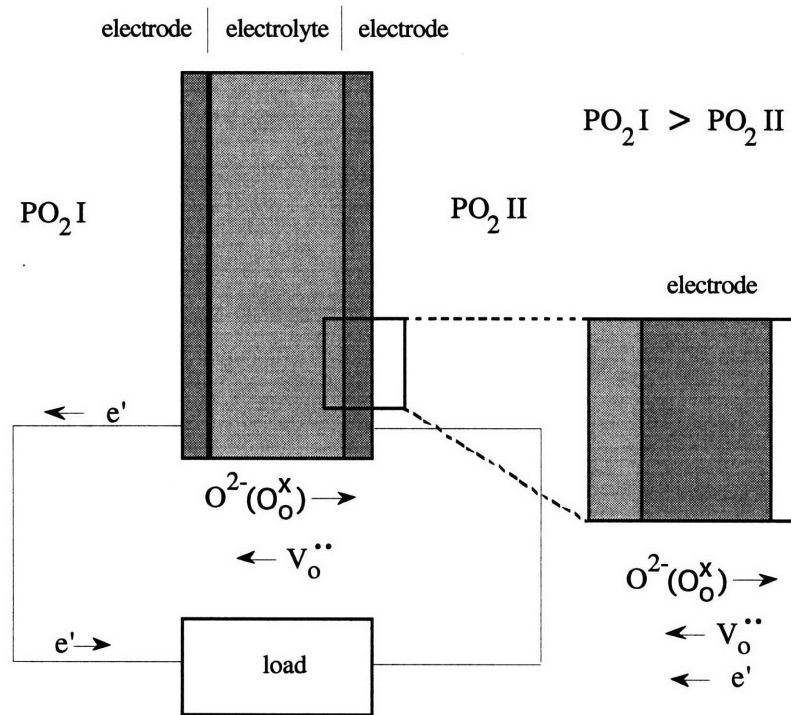
Figure 1: A schematic diagram of a simple parallel plate solid oxide fuel cell (SOFC). A gradient in the partial pressure of oxygen drives the oxygen ions and the

oxygen vacancies through the electrolyte. The electrodes must be mixed
conductors. Schematic modified from (ref. 10).

The electrode may also be constructed out of a ceramic material. It must have an identical
coefficient of thermal expansion suggesting that it would be ideal to use the same material as
used for the electrolyte. Furthermore the use of such a similar material might reduce the
interfacial impedance between the electrolyte and the electrodes, thus improving the conductivity
of the overall device. However, unlike the electrolyte, the electrodes must be mixed conductors
so that the oxidation and reduction reactions may take place at the anode and cathode
respectively, and DC current may be drawn from the cell.

By studying the effects of doping on nanocrystalline cerium oxide, we have sought to
understand the effect of grain size on the conductivity and the conduction mechanism. An
understanding of any such size-effects on the behavior of the doped material may lead to the
creation of practical components for SOFC's, but, more importantly, will help to elucidate size
effects in general for oxides.

2.2 Characterization Techniques

2.2.1 X-ray Line Broadening

X-ray line broadening analysis is a simple method for determining the volume-weighted
mean crystal diameter or grain size for nanocrystalline materials. In crystalline materials with
mean crystal diameters less than 500 nm, peak broadening of the x-ray diffraction (XRD)
spectra will occur. Cullity[11] describes this very clearly. Bragg's law describes the geometrical
relationship between the x-ray beam angle of incidence at which diffraction occurs, θ, and the
spacing between the parallel planes in the crystal, d, as follows:

$$n\lambda = 2d\sin\theta \qquad\qquad \text{Eq. 2}$$

where λ is the wavelength of the x-rays. This equation holds true for an infinitely large crystal
and implies that for such a crystal, the peaks will be infinitely narrow, existing only at specific
thetas, or Bragg angles, associated with specific d-spacings. However, for very small crystals,
there will not be enough parallel planes within any crystal to lead to destructive interference at
every angle except the Bragg angle. Thus, diffraction will occur at angles near the Bragg angle,
and the peaks will broaden. As the crystals become smaller, there will be even fewer planes
available for destructive scattering, and diffraction will occur at more thetas near the Bragg angle

10

leading to further broadening. The relationship between this peak broadening, or angular divergence, and crystal size is represented by Scherrer's formula:

$$d_g = \frac{0.9\lambda}{B\cos\theta_B}$$

Eq. 3

Where d_g is the mean crystal diameter, B is the full width half maximum of the peak (in radians), λ is the wavelength of the x-rays (1.54 Å for copper K_α radiation, the most commonly used) and 0.9 is a factor which derives from an exact treatment of the derivation which is not discussed here. The full width half maximum, B, is the result after subtracting the instrument line broadening from the total line broadening. It should be noted that while Scherrer's formula gives one a reasonable value of the grain or particle size of the material, it does not account for the residual stress in the material which may be induced during such processing as hot-pressing of a pellet. There are formulas which can separate out the strain and crystal size of a material, but they require extremely good data and more analysis.

In this work, several of the values obtained via Scherrer's formula have been confirmed through microscopy. From these results, then, it appears that Scherrer's formula as applied to x-ray line broadening results is sufficiently accurate.

2.2.2 Impedance Spectroscopy

Macdonald[12] provides a good overview of impedance spectroscopy and its applications for the study and characterization of the electrical properties of solids. Impedance spectroscopy is an attractive technique because it can be used to separate out the different contributions to conduction within a material. Each of these contributions may be modeled as an element or elements in an equivalent circuit. There are several equivalent circuit models for ceramic materials including the Voigt and the Maxwell models. As Macdonald notes, Bauerle[13] adapts the Voigt model to polycrystalline ceramics leading to the equivalent circuit depicted in figure 2:

11
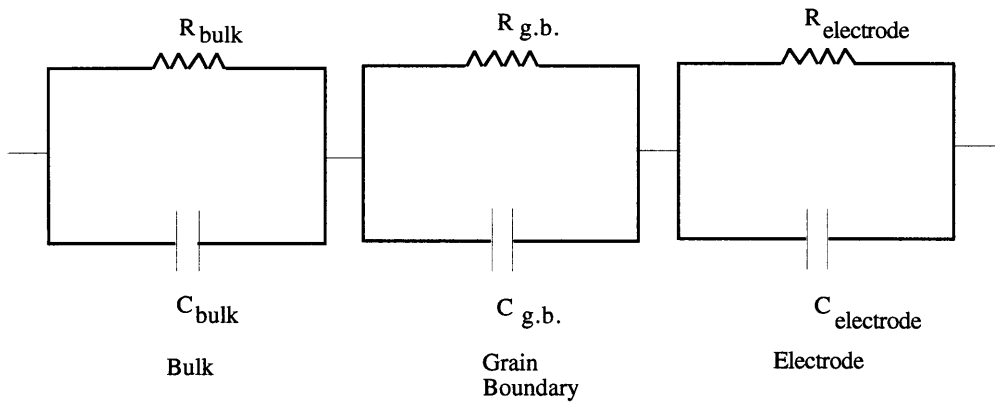
Figure 2: The Voigt equivalent circuit model applied to polycrystalline materials. It is composed of three RC circuits representing the bulk of the material, blocking grain boundaries, and blocking electrodes.

Each of the RC circuits has an associated time constant which is correlated with the electrical processes in the material. These include the movement of charged carriers to the electrodes, the movement of carriers about the grain boundaries, and the movement of carriers within the perfectly ordered lattice. The application of the Voigt model in this manner is based upon the presence of perpendicular grain boundaries and blocking electrodes. Blocking electrodes are those which do not conduct the carriers in the sample, or electrolyte, so that charge builds up at the electrode interfaces. Perpendicular grain boundaries, or blocking boundaries, are represented by the grain boundary element and are those which are oriented perpendicular to the path of conduction through the material. Since they are regions of highly disordered material, they tend to impede the flow of charge. It should be emphasized that the grain boundary component of this model does not account for the effect of parallel grain boundaries, since in model polycrystalline materials, the parallel grain boundaries account for a very small portion of the sample. However, such boundaries may account for a significant portion of the cross-section of the material in nanocrystalline samples, and we believe that the effect of any contributions would then appear in the bulk component of the model.

$R_1 = R_{bulk}$

$R_2 = R_{bulk} + R_{g.b.}$

$R_3 = R_{bulk} + R_{g.b.} + R_{electrode}$
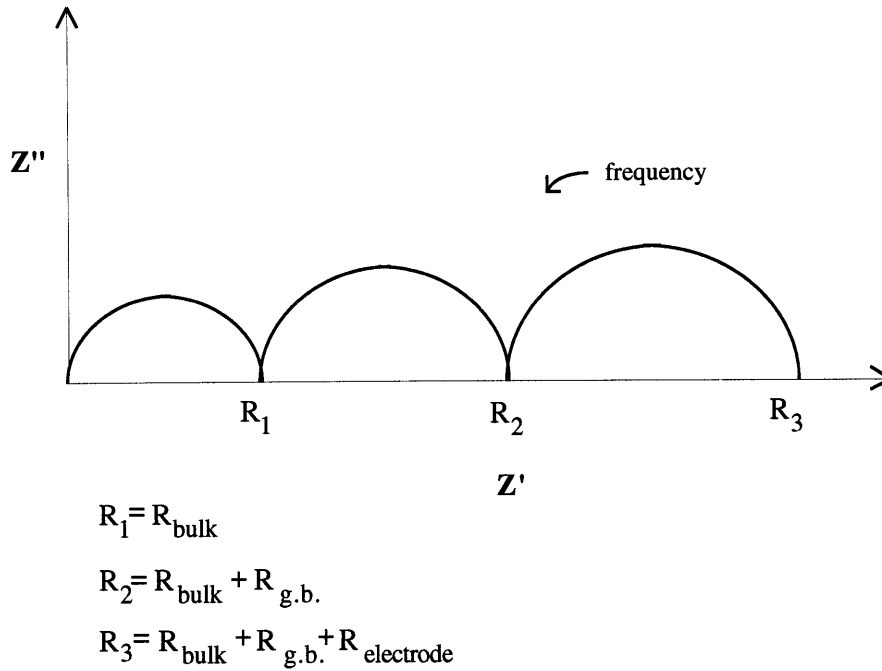
Figure 3: An ideal impedance plot. Each of the semicircles is correlated with an RC circuit. In practice, the arcs are rarely so well defined, and one must interpolate to determine the appropriate arcs.

Figure 3 depicts the three arcs of an ideal impedance plot associated with the Voigt equivalent circuit. The technique of impedance spectroscopy involves varying the frequency of an AC signal over a wide range (typically from 1 Hz to 1 Mhz). A single RC circuit produces an arc in the complex impedance plot. The intersection of the right side of the arc is associated with the resistance of that element, and the top of the arc is associated the time constant of the element. Assuming that the different elements associated with the material have different time constants, the resulting ideal impedance plot will have well separated arcs.

The time constants are related to the differences in the response of the components of the material. Thus, by sweeping the frequency, one should be able to separate out the components that give rise to conduction in the material based on their ability to respond. The bulk will have the least delay because the carriers will be able to move very quickly trough the ordered lattice. The carriers at the grain boundaries will move more slowly because of scattering due to the disorder in the region. The carriers at the electrode interface will move the most slowly such that they will only respond at the lowest frequencies, because the interface between the electrode and

the sample tends to be extremely disordered. As a result, at the lowest frequencies, one will see the total impedance of the sample, but as the frequency is increased, one will only measure the complex impedance of the elements of the sample that are capable of responding at higher frequencies. In practice, the arcs are rarely so well defined. If the time constants of the sections of the material are similar, then overlap between the two arcs will occur. The spectrum can be deconvoluted to determine the resistance and then the conductivity of the bulk and grain boundary components of the material.

2.3 Contributions to Conduction in Oxides

Conduction occurs in a material due to the net movement of charged carriers. In cerium oxide, the most prominent carriers are electrons and singly or doubly ionized oxygen vacancies[14]. Conductivity is the product of the number of carriers in a material, their charge, and their mobility as shown in equation 4 for electrons:

$$\sigma_n = ne\mu_n \qquad \text{Eq. 4}$$

where σ_n is the conductivity of the carriers, in this case, electrons, n is the concentration of electrons, e is the charge on an electron, and μ_n is the mobility of an electron. The number and mobility of the conducting species are dependent upon the structure, temperature, and nonstoichiometry of the material which depends on the atmosphere and temperature. Cerium oxide is readily reduced to a wide range of nonstoichiometries due to the crystal structure and multiple valence states of the cerium ion.

Tuller and Nowick[15] have shown that cerium oxide is a small polaron conductor, meaning that the electrons are localized and hop from one site to the next. This behavior is particularly important in reference to conduction in the nanocrystalline material, because it follows that if the mobility is based on a localized behavior, it should not be a function of grain size. This implies that only the carrier concentration will scale with the conductivity as a function of grain size. The mobility, as determined by Tuller and Nowick[15], is an activated process described by the following equation:

$$\mu_e = \left(\frac{\mu_o}{T}\right)\exp\left(-\frac{E_h}{kT}\right) \qquad \text{Eq. 5}$$

14

where E_h is the hopping energy for mobility equal to 0.4 eV for small deviations from stoichiometry. Blumenthal and Hoffmaier[16] arrived at a similar result using sintered specimens over a temperature range of 300°C to 1000°C.

Having considered the mobility, one should consider the concentration and behavior of the defects that lead to conduction. Tuller and Nowick[14] considered the possible defect reactions as applied to ceria using Kroger-Vink notation for small deviations from stoichiometry. They are:

$$O_O^x \rightarrow V_O^{\bullet\bullet} + 2e' + \tfrac{1}{2}O_2(g) \qquad \text{Eq. 6}$$

$$V_O^{\bullet} \rightarrow V_O^{\bullet\bullet} + e' \qquad \text{Eq. 7}$$

$$V_O \rightarrow V_O^{\bullet} + e' \qquad \text{Eq. 8}$$
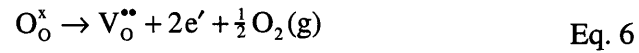
These reactions describe the primary reactions for the formation of carriers in pure cerium oxide. The mass action relations that are related to these equations follow:

$$[V_O^{\bullet\bullet}]n^2 PO_2^{\frac{1}{2}} = K_1(T) = K_{10}\exp(-H_1 / kT) \qquad \text{Eq. 9}$$

$$[V_O^{\bullet\bullet}]n / [V_O^{\bullet}] = K_2(T) = K_{20}\exp(-H_2 / kT) \qquad \text{Eq. 10}$$

$$[V_O^{\bullet}]n / [V_O] = K_3(T) = K_{30}\exp(-H_3 / kT) \qquad \text{Eq. 11}$$

for which $K_i(T)$'s are the temperature dependent equilibrium constants and H_i's are the enthalpies associated with the reactions. These equations can be combined with the electroneutrality condition:

$$n = [V_O^{\bullet}] + 2[V_O^{\bullet\bullet}] \qquad \text{Eq. 12}$$

to solve for the defect concentration as a function of the equilibrium constants and PO_2. The result is:

$$n^3 - K_1(T)PO_2^{-1/2}\left(\frac{n}{K_2(T)} + 2\right) = 0 \qquad \text{Eq. 13}$$

which is obtained via the simultaneous solution of equations 9-12.

There are two limiting cases based on these relationships. The first assumes the formation of doubly ionized oxygen vacancies, which occur at moderate temperatures and high

oxygen partial pressures, such as those encountered in this work. For intrinsic conduction with doubly ionized vacancies, the following approximation applies:

$$2[V_O^{..}] = n \qquad \text{Eq. 14}$$

where the concentration of carriers is thermally activated. This equation, combined with equation 9 leads to the relationships:

$$n \propto Po_2^{-1/6} \qquad \text{Eq. 15}$$

for constant temperature, and

$$n \propto K_R(T)^{-1/3} \qquad \text{Eq. 16}$$

for constant oxygen partial pressure where K_R is the equilibrium reduction constant for this case.

There are always a certain number of impurities in these ceramic materials, so that even for the "pure" cerium oxide, one will encounter the effects of doping at very low temperatures and high oxygen partial pressures. For the doped materials, or for the pure materials under these conditions, the following defect relation will hold:

$$2[A'] = [V_O^{..}] \qquad \text{Eq. 17}$$

which implies that the number of oxygen vacancies is fixed over a wide range of oxygen partial pressures (PO_2's). Thus the number of electrons in the system will be independent of the oxygen vacancy concentration and the electron concentration will scale as:

$$n \propto Po_2^{-1/4} \qquad \text{Eq. 18}$$

for constant temperature and

$$n \propto K_R(T)^{-1/2} \qquad \text{Eq. 19}$$

for constant PO_2. The equilibrium constant is related to the enthalpy of reduction (H_R) in the following manner:

$$K_R = \exp(-H_R/kT) \qquad \text{Eq. 20}$$

so that for intrinsic behavior with doubly ionized vacancies,

$$\frac{\partial \log n}{\partial(1/T)} = \frac{-H_R}{3} \qquad \text{Eq. 21}$$

and for the extrinsic behavior with doubly ionized vacancies,

16

$$\frac{\partial \log n}{\partial (1/\ T)} = \frac{-H_R}{2}$$

<div align="right">Eq. 22</div>

The second limiting case occurs when all of the oxygen vacancies are singly ionized. This occurs at very low oxygen partial pressures and at very high temperatures. Following the outline for the doubly ionized work:

$$[V_O^{\cdot}] = n$$

<div align="right">Eq. 23</div>

for the intrinsic region so that,

$$n \propto Po_2^{-1/4}$$

<div align="right">Eq. 24</div>

for constant temperature, and

$$n \propto K_R^{'}(T)^{-1/2}$$

<div align="right">Eq. 25</div>

for constant PO_2 where $K_R{'}$ is the equilibrium reduction constant for singly ionized vacancies. For the extrinsic region,

$$[A'] = [V_O^{\cdot}]$$

<div align="right">Eq. 26</div>

so that

$$n \propto Po_2^{-1/2}$$

<div align="right">Eq. 27</div>

for constant temperature, and

$$n \propto K_R^{'}(T)^{-1}$$

<div align="right">Eq. 28</div>

for constant PO_2. Since the reduction constant is related exponentially to the reduction enthalpy as shown in equation 20, the concentration of carriers is related in the following way:

$$\frac{\partial \log n}{\partial (1/\ T)} = \frac{-H_R^{'}}{2}$$

<div align="right">Eq. 29</div>

for the intrinsic region and by

$$\frac{\partial \log n}{\partial (1/\ T)} = H_R^{'}$$

<div align="right">Eq. 30</div>

for the extrinsic region. By determining the dependence of the concentration of carriers on the PO_2 and temperature, one can predict the ionization of the vacancies and the enthalpy of reduction at the extremes.

A transition must occur between these two extreme cases of all singly or all doubly ionized vacancies. Tuller and Nowick, in their paper calculate it to be:

<div align="center">17</div>

$$PO_2 = 1.91 \times 10^{10} \exp(-6.00 eV / kT) \qquad \text{Eq. 31}$$

This transition has been confirmed by Blumethal et al.[17].

2.4 Theoretical Calculations Regarding the Heat of Reduction for Different Ceria Surfaces

Sayle et al.[18] applied computer simulation techniques to determine the energies associated with the catalysis of CO_2 over cerium oxide. As part of their calculations, they determined the energy associated with the formation of oxygen vacancies on the various crystal surfaces of cerium oxide through the following defect reaction:

$$O_O^X + 2Ce_{Ce}^X \rightarrow \tfrac{1}{2}O_2(g) + V_O^{\cdot\cdot} + 2Ce_{Ce}^{\prime} \qquad \text{Eq. 32}$$
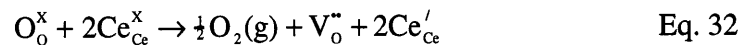
Their calculations are based on the formation of a single, doubly ionized oxygen vacancy in a perfect, defect free surface. Table 1 summarizes the results:

Table 1: Calculated energies associated with the formation of oxygen vacancies on different surfaces in cerium oxide

Surface	Energy for formation of a single, doubly ionized oxygen vacancy (eV)
bulk	6.58
(111)	2.71
(110)	-0.47
(310)	-6.25

As a point of comparison, the experimentally determined value for the bulk enthalpy of reduction for pure single crystal cerium oxide is 4.67 eV, as measured by Tuller and Nowick[14]. Considering the variation between the calculated and experimentally determine values, it appears that the calculations do not give accurate absolute values, but they are valuable in that they demonstrate the differences in oxygen vacancy formation for different surfaces of ceria. The negative values for the formation of vacancies is correlated with spontaneous formation of vacancies on those surfaces. The idea that there are differences in enthalpy of reduction at the different surfaces can be extended to the grain boundaries. This suggests that different grain boundary sites will exhibit different oxygen vacancy formation energies, and there will be a spectrum of vacancy formation energies throughout a sample.

3. Experimental

3.1 Synthesis

3.1.1 Powder Synthesis

The solutions were prepared using high-purity (99.999%) cerium acetate and gadolinium acetate (Johnson Matthey) and at least 17.6 M-ohm deionized water (Millipore). Appropriate amounts of acetates were massed to produce approximately 5 grams of final powder of the desired composition. The acetates were added to the water, the beaker was covered with aluminum foil to reduce contamination, and the solution was stirred with a teflon-coated magnetic stir bar. All labware in contact with the solution was either polypropylene or teflon-coated to reduce metal and silica contamination.

Stirring was continued for a few hours for the pure material and for several hours for the doped material. All of the solutions went from being cloudy to clear within minutes of commencement of stirring. Following stirring, the solution was decanted and atomized into liquid nitrogen. The liquid nitrogen boiled off to leave a fine crystalline substance that was spread on clean aluminum foil in the freeze-drier and placed under vacuum. The temperature of the freeze-drier shelf was raised over the course of several of days from -40 °C to room temperature.

After freeze-drying, the powder was placed in covered but ventilated alumina boats and calcined for two hours just above the highest decomposition temperature determined from the thermal gravitational analysis (TGA) (300 °C for the pure material, and 500 °C for the doped material). Subsequently, the powder was degassed in a vacuum oven for at least 48 hours and then stored in a dry box.

3.1.2 Pellet Densification and Heat Treatments

A small amount of the powder (approximately 0.2 grams) was loaded into a tungsten-carbide cobalt apparatus in a nitrogen-filled dry box to reduce the amount of physabsorbed species and densified at approximately 650 °C and 0.8 GPa. The apparatus creates a reducing environment at 650 °C, so that the nanocrystalline pellets appeared dark grey upon removal from the die. Heating at 400 °C for one hour in air oxidized the pellets and caused them to become light yellow in color.

All of the heat treatments were performed in a tube furnace in air. The samples were placed on platinum foil in an alumina boat in a new alumina tube to reduce the possibility of contamination. The temperatures reported were measured via a thermocouple placed adjacent to, but not in, the alumina tube with the sample.

3.2 Characterization of Samples

The powder and pellets were characterized using a variety of techniques. The powder phase and particle size were characterized using XRD (Rigaku rotating anode x-ray generator). Both the powder and the pellets were further characterized using high-resolution transmission electron microscopy (HREM) (Topcon, 002B). Field emission scanning electron microscopy (FESEM) was performed on fracture surfaces of some of the samples to analyze the grain size and porosity. Archimedes measurements were performed on the samples, as well as on other, similarly processed samples, using 35 gauge copper wire in deionized water.

3.3 Electrical Measurements

Electrical measurements were performed using a Hewlett Packard 4192-LF impedance spectrometer. Platinum was sputtered on the surfaces for electrodes using DC magnetron sputtering. After sputtering, the samples were cleaned and loaded into our sample holder, shown in figure 4. The holder consists of a quartz tube which is sealed on both ends with cajon fittings allowing for atmosphere control. The central tubes are alumina and contain the platinum-rhodium leads.

The platinum-rhodium leads were coiled into springs and capped with platinum mesh so that good electrical contact was maintained with the sample as the sample was heated and cooled. Initially, we tried to measure the samples without the spring construction, but we found that the samples tended to crack and fall apart upon removal from the holder. We believe that this was due to the force placed on them as a result of the differences in the coefficients of thermal expansion for the alumina and quartz tubes. The springs allowed for good electrical contact without compromising the sample integrity.

length of furnace: 12 inches

diameter of sample: approx. 6.2 mm
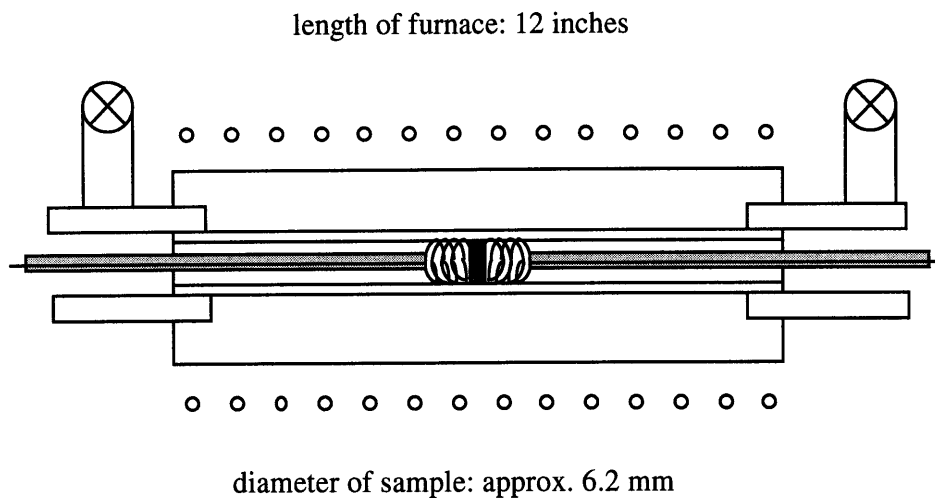
Figure 4: A schematic of the sample holder used for the electrical measurements shown with a sample in the furnace.

The temperature was measured and controlled using a type K thermocouple set just outside the quartz sheath of the sample holder at the sample location. The oxygen partial pressure was created via premixed oxygen-argon mixtures and compressed air. Measurements were taken over a series of hours and days to assure that the samples were equilibrated. Measurements were taken such that data was collected for a set of temperatures as the sample was heated, and then the sample was studied at intermediate temperatures upon cooling.

4. Results and Discussion

4.1 Characterization of the Samples

The Archimedes measurements showed that all of the samples have densities greater than 90% of the theoretical value. Table 2 summarizes the sample heat treatments and grain sizes.

Table 2: A Summary of the Sample Heat Treatments and Grain-Sizes

Sample	Treatment	Grain size
n-CeO_{2-x}	as densified	$d_g \sim 13$ nm [1,2]
n-$Ce_{0.9823}Gd_{0.0177}O_{2-x}$	as densified	$d_g \sim 13$ nm [2]
a1-CeO_{2-x}	700 °C for 3 hours	$d_g \sim 16$ nm [1]
a2-CeO_{2-x}	700 °C for 1 hour	$d_g \sim 14$ nm [1]
c1-CeO_{2-x}	990 °C for 1 hour	$d_g \sim 83$ nm [1]
c2-CeO_2	1200 °C for 4 min	$d_g \sim 100$ nm-1 μm [3]

[1] Scherrer's formula applied to XRD results
[2] HREM
[3] FESEM

For the HREM work, samples were prepared in the identical manner to those used in the electrical measurements and then characterized. HREM was used to confirm the grain size of the as-densified samples, n-CeO_{2-x}, and n-$Ce_{0.9823}Gd_{0.0177}O_{2-x}$. Figure 5 is a micrograph of an as-densified sample showing the extremely fine grain size, as well as an absence of grain boundaries films which would have a significant impact on the electrical properties of the material.
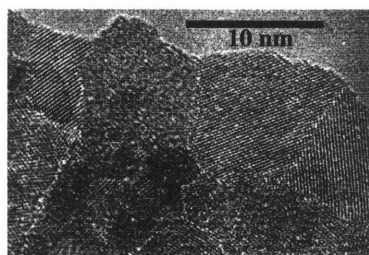
Figure 5: An HREM image of a sample of the as-densified cerium oxide confirming the extremely fine grain size ($d_g \sim 13$ nm) as determined via x-ray line broadening analysis and also showing an absence of and amorphous films at the boundaries. (courtesy of Dr. Harold Ackler)

Annealing at 700 °C for one hour has virtually no effect on the grain size, as can be seen by comparing the grain size of the samples a1-CeO_{2-x} and a2-CeO_{2-x} with the nanocrystalline sample n-CeO_{2-x}. Slight variations within data gathered via the application of Scherrer's formula to x-ray line-broadening data are to be expected. Hence, these samples are considered to be annealed but not coarsened. In contrast, the coarsened samples, c1-CeO_{2-x}, and c2-CeO_2, have significantly lower specific surface areas. The specific surface area is the ratio of surface area or

interface area to volume and is proportional to the inverse of the grain size. The specific surface area is defined in the following way for polycrystalline materials assuming a tetrakaidecahedron grain structure[19]:

$$S_v = \frac{3.5513}{d_g} \qquad \text{Eq. 33}$$

where S_v is the specific surface area, d_g is the mean crystal diameter, and 3.5513 is a factor that arises from the assumption of a tetrakaidecahedron grain structure. Using this relation, one can see that the specific surface area for the annealed sample, $a1\text{-}CeO_{2-x}$ is over five times greater than that for the moderately coarsened sample, $c1\text{-}CeO_{2-x}$. The grain size of the coarsest sample, $c2\text{-}CeO_{2-x}$, was characterized via FESEM which revealed a bimodal grain size distribution with fine grains of 100 nm interspersed with larger grains of approximately 1 μm in diameter as shown in figure 6.
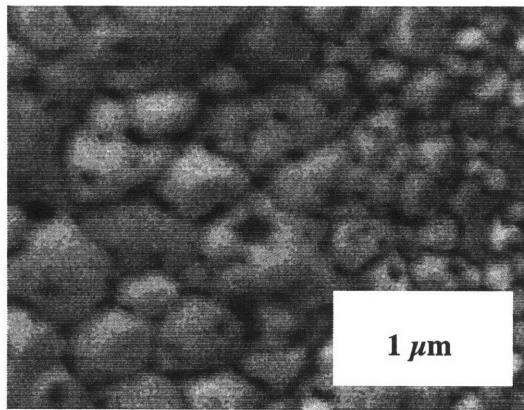
Figure 6: A FESEM micrograph of the coarsest sample, $c2\text{-}CeO_2$ which shows the bimodal distribution (100 nm - 1 μm) of grain sizes as well as limited, closed porosity.

Figure 6 also shows what appears to be limited residual porosity, but it appears to be closed, and thus, it is not expected to impact the electrical results.

4.2 Impedance Spectroscopy: Typical Spectra

Figure 7 shows a typical spectrum for the as densified sample, $n\text{-}CeO_{2-x}$. It exhibits two arcs, the "bulk" arc, and the "boundary" arc. In this case, the "boundary" arc is not shown or labeled due to its small size compared to the "bulk" arc. The term for the "bulk" and "boundary" are in quotations, because certain boundary effects, such as that of parallel conduction may not be represented by the "boundary" arc, but may instead be represented by the "bulk" arc. Note

that there is no electrode arc. We have not seen an electrode arc for any of the samples. We attribute this to ohmic contacts between the platinum and the ceria.
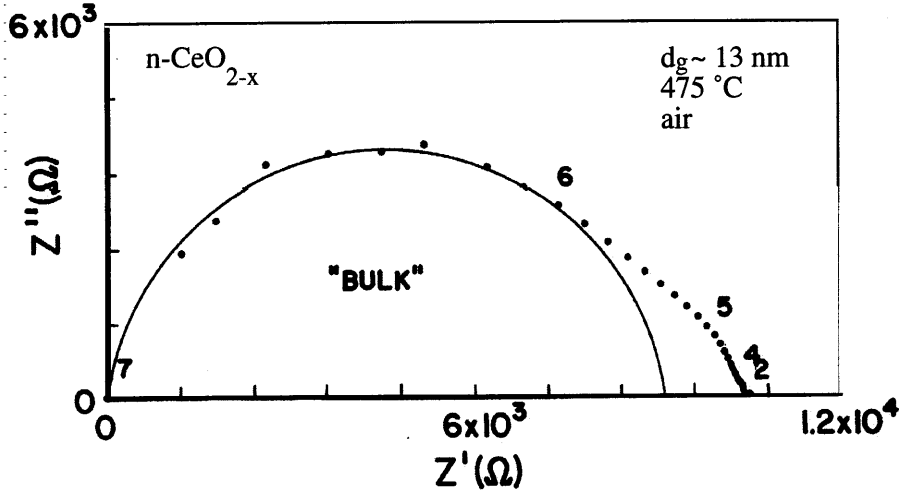
Figure 7: A typical spectrum for the as densified sample, $n\text{-}CeO_{2-x}$. The spectrum is dominated by the "bulk" arc.
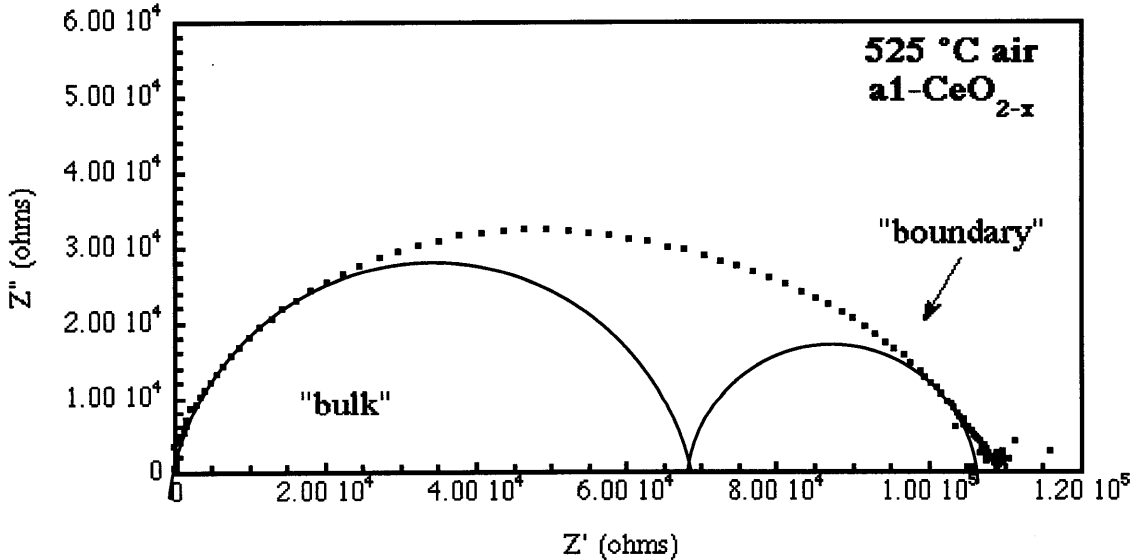
Figure 8: A typical impedance spectrum for the annealed sample, $a1\text{-}CeO_{2-x}$, showing both the "bulk" and the "boundary" arcs. "Bulk" and "boundary" are in quotations to emphasize the fact that bulk arc may include effects of parallel boundaries. There is no electrode arc, which is consistent with ohmic contacts on electronic conductors.

Figure 8 shows a typical impedance plot for the annealed sample, $a1\text{-}CeO_{2-x}$. Once again, there are two major arcs: the "bulk" arc, and the "boundary" arc, but the ratio of the "boundary" arc to

the "bulk" arc is larger than that for the sample n-CeO$_{2-x}$. The ratio of the "boundary" to the "bulk" arc becomes larger as the sample is coarsened, as shown in figure 9.
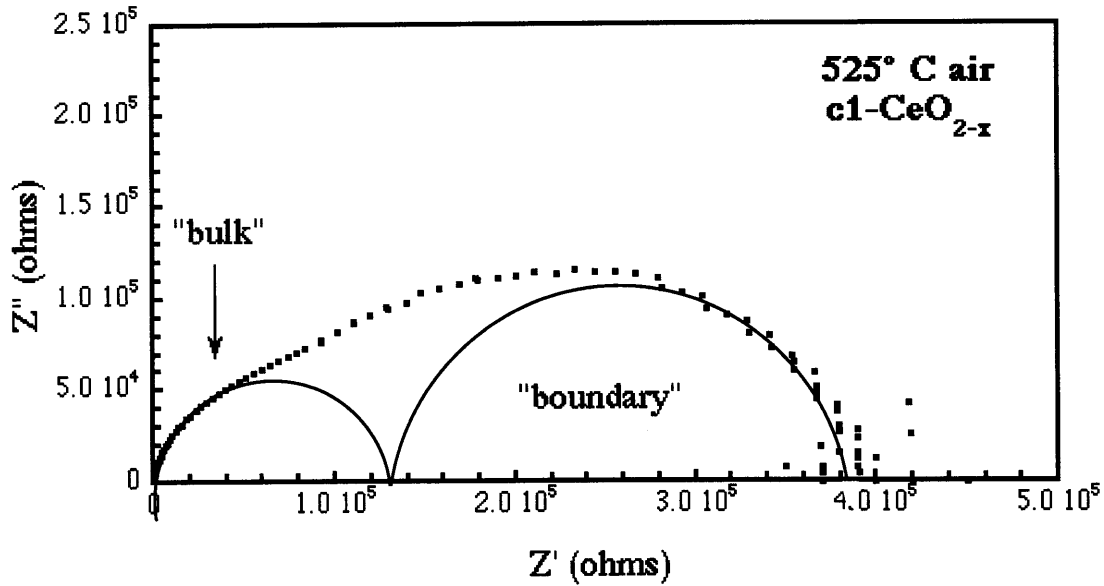
Figure 9: A typical impedance spectrum for the coarsened sample, c1-CeO$_{2-x}$, which exhibits a grain size of 83 nm and is moderately coarsened. Notice that the "boundary" arc is larger than the "bulk" arc.

The "boundary" arc is significantly increased with respect to the "bulk" arc. This trend, though, is not continued with the coarsest sample, c2-CeO$_2$ which exhibits arcs of similar size as shown in figure 10.
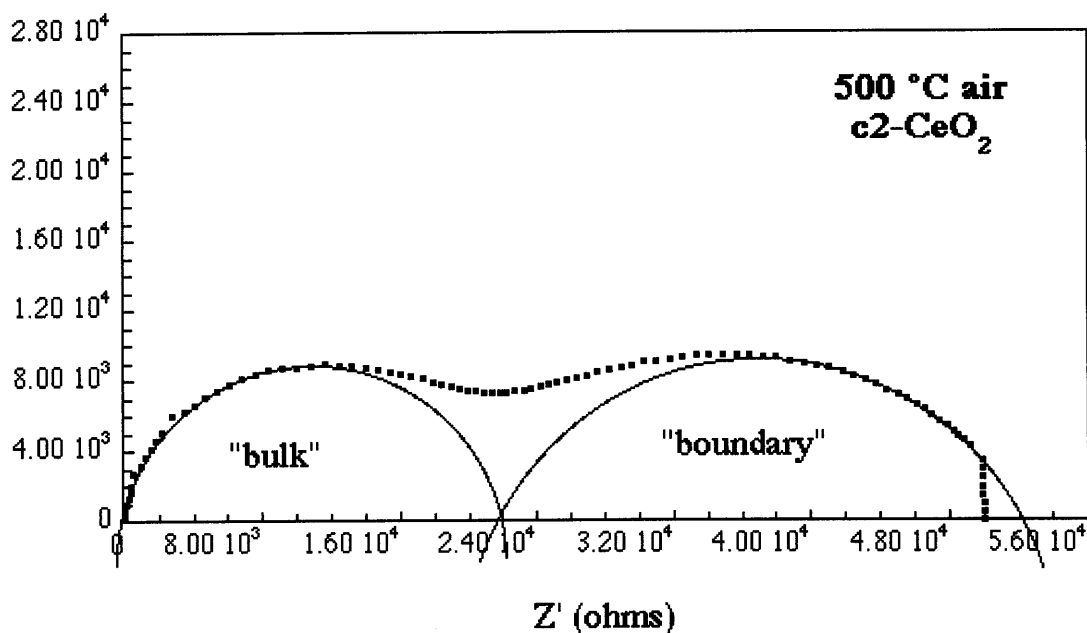
Figure 10: A typical spectrum for the coarsest sample c2-CeO$_2$ showing the "bulk" and "boundary" arcs.

The variation in grain boundary impedance with grain size for the samples n-CeO$_{2-x}$, a1-CeO$_{2-x}$, and c1-CeO$_{2-x}$ is most likely due to size-dependent impurity segregation[20,21,22]. The segregation leads to changes in the character of the boundaries, making the boundaries more conductive when more of the solute segregates at the smaller grain sizes. However, as the sample coarsens, it appears that the nature of the grain boundaries become relatively constant because size dependent segregation has only been seen in the very fine-grained regime[20,21,22]. Thus, the boundary arc and corresponding boundary resistance will decrease, because the number of such boundaries will decrease with increasing grain size. Hence, the ratio of the "boundary" to the "bulk" arc for the sample c2-CeO$_2$ is smaller than that for c1-CeO$_{2-x}$. In order to understand changes in defect thermodynamics with size scale and heat treatment, we focus on the high-frequency arc.

4.3 Time Dependence Results

Figure 11 depicts the variation in resistance with time as the annealed sample, a1-CeO$_{2-x}$ is cooled from 500 °C to 450 °C in air. The furnace was set to cool at a rate of 1.67 degrees per minute. Thus, in the plot, the data shown before time zero was taken during the cooling time,

and the point at time zero marks the resistance at the time when the furnace reached 450 °C. The total resistance was determined by the intersection of the spectrum with the real axis, and the values for the "bulk" and "boundary" reisistances were determined by deconvolution of the spectrum. The sample equilibrates quickly, with most of the equilibration occurring during the time taken to slowly cool the sample. We waited until we were sure that the data was time-invariant before changing conditions.
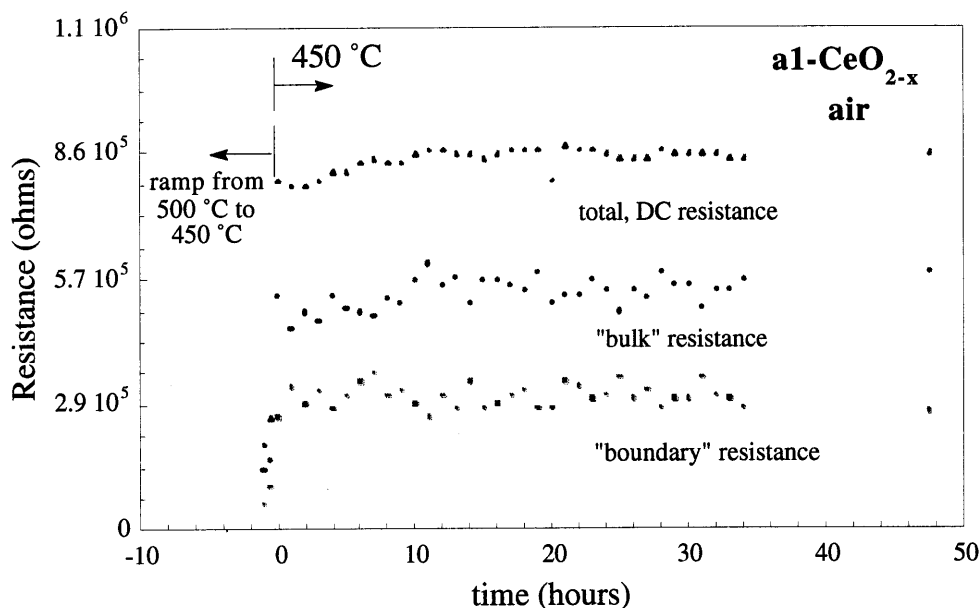
Figure 11: A plot of the dependence of the resistance for the sample a1-CeO_{2-x} as a function of time. This plot demonstrates the speed at which the sample achieves time-invariant behavior.

4.4 The Conductivity of Pure, Nanocrystalline Cerium Oxide

Figure 12 shows the temperature dependence of the conductivity for the as-hot pressed sample, n-CeO_{2-x}, which exhibits an activation energy of 1.16 eV. As described in the section on the contributions to conduction in oxides, the activation energy is related to the enthalpy of reduction based on the choice of the model for conduction. Since these experiments were performed at moderate temperatures and high oxygen partial pressures, the oxygen vacancies were doubly ionized[14] implying the following defect reaction for reduction:

$$O_O^x + 2Ce_{Ce}^x \Leftrightarrow \tfrac{1}{2} O_2(g) + V_O^{\bullet\bullet} + 2Ce_{Ce}' \qquad\qquad \text{Eq. 34}$$

27
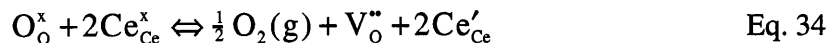
so that the enthalpy of reduction for this sample is contingent only on whether the material is intrinsically conducting where the electroneutrality condition is $n=2[V_O^{\bullet\bullet}]$, or whether it is extrinsically conducting, where there are sufficient background impurities to pin the oxygen vacancy concentration so that $[A_{Ce}']=2[V_O^{\bullet\bullet}]$. For the intrinsic regime, the slope of the log σ-log PO_2 plot should be -1/6, and for the extrinsic regime, the log σ-log PO_2 plot should show a -1/4 dependence.
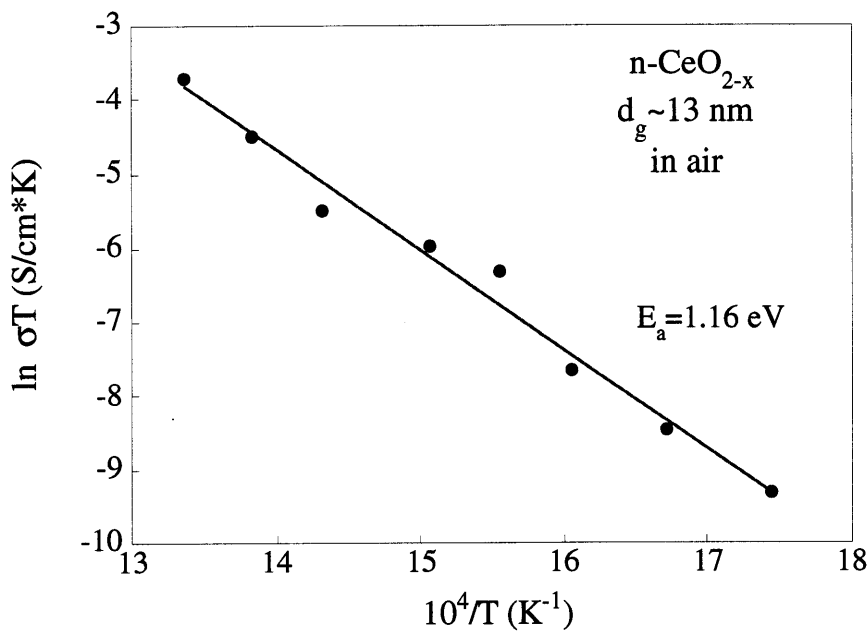
Figure 12: The variation in conductivity with temperature for n-CeO_{2-x}. The sample exhibits enhanced conductivity and a lower activation energy than that of the single crystal or traditional polycrystalline reduced cerium oxide.

Therefore, to determine the enthalpy of reduction, one must determine the PO_2 dependence as shown in Figure 13.
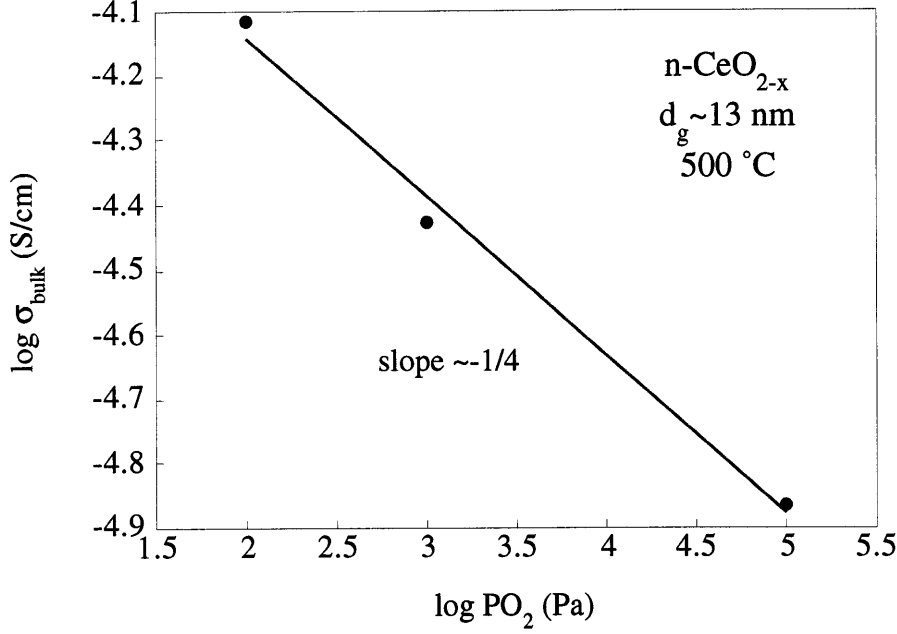
Figure 13: The dependence of the conductivity on the partial pressure of oxygen for n-CeO$_{2-x}$. The slope is approximately -1/4, suggesting extrinsic behavior, but both the results for intrinsic and extrinsic behavior are considered in the comparison of the heat of reduction for this sample with other, more conventional samples.

The PO$_2$ dependence is approximately -1/4, suggesting extrinsic reduction, but rather than only calculating the heat of reduction for the extrinsic case, we have calculated it for both cases, to give a more complete and less biased analysis.

Recalling that CeO$_{2-x}$ is a small-polaron conductor[15], electronic conductivity is given by

$$\sigma_e = ne\mu_e = ne\left(\frac{\mu_o}{T}\right)\exp\left(-\frac{E_h}{kT}\right)$$
Eq. 35

where σ_e is the electronic conductivity, n is the carrier concentration, e is the charge on the carrier, and μ_e is the carrier mobility, which is simply a reexpression of equations 4 and 5. It exhibits an activated mobility with a hopping energy, E_h, of 0.4 eV[15]. The defect reaction in equation 33 has an equilibrium constant of the form[23]:

$$K_1(T) = K_1^o \exp\left(-\frac{\Delta H_1}{kT}\right) = [V_O^{\cdot\cdot}]n^2 Po_2^2$$
Eq. 36

29

where K_1^0 is a constant and ΔH_1 is the enthalpy of reduction per $V_O^{..}$. Thus for intrinsic reduction, where electroneutrality is given by $n=2[V_O^{..}]$, the activation energy is defined as

$$E_a=(\Delta H_1/3)+E_h \qquad \text{Eq. 37}$$

Likewise, for extrinsic reduction, the electroneutrality condition is $[A_{Ce}']=2[V_O^{..}]$, and the activation energy is

$$E_a=(\Delta H_1/2)+E_h \qquad \text{Eq. 38}$$

The calculated values for the enthalpy of reduction are listed in Table 3.

Table 3: Volume Heat of Reduction for n-CeO_{2-x} as compared with published values for more conventional cerium oxide

Sample	E_a(eV)	ΔH_R (eV per $V_O^{..}$)	
		intrinsic, $n = 2[V_O^{..}]$	extrinsic, $[A_{Ce}'] = 2[V_O^{..}]$
n-CeO_{2-x}	1.16	2.28	1.52
Reduced single crystal[14]	1.96	4.67	
Acceptor-doped polycrystals[24]	2.37		3.94

The enthalpy of reduction is over 2 eV lower than that for conventional ceria regardless of the reduction mechanism. We believe that this low enthalpy of reduction results from the presence of low energy defect formation sites at the interfaces which arise due to the greater degree of disorder at the grain boundaries than in the center of the grains. Nanocrystalline material is dominated by interfaces. The low energy defect formation sites at the interfaces lead to the formation of a large number of defects, thus enhancing the conductivity of the oxide and causing it to appear reduced in a region in which conventional material is not able to equilibrate[14].

4.5 The Effect of Annealing without grain coarsening on the Electrical Properties: a1-CeO_{2-x} and a2-CeO_{2-x}

The data regarding the nanocrystalline sample suggests that at the nanocrystalline size-scale there are unique properties: higher conductivity than is observed in conventional ceria, reduced behavior in regimes where extrinsic behavior is normally observed, and a lower enthalpy of reduction. We probed the variation in conductivity with heat-treatments which did not lead to coarsening to determine the stability of this behavior.

Figure 14 shows the dependence of the conductivity with temperature for the annealed samples, a1-CeO_{2-x}, and a2-CeO_{2-x}, as compared with the nanocrystalline sample, n-CeO_{2-x}. Recall that both of the annealed samples were heat treated at 700 °C and are virtually uncoarsened.

in air

n-CeO_{2-x}
(d_g ~13 nm)
$E_a = 1.16$ eV

a1-CeO_{2-x}
(d_g ~ 16 nm)
$E_a = 1.40$ eV

a2-CeO_{2-x}
(d_g ~ 14 nm)

y-axis: ln σT (S/cm*K)

x-axis: $10^4/T$ (K^{-1})
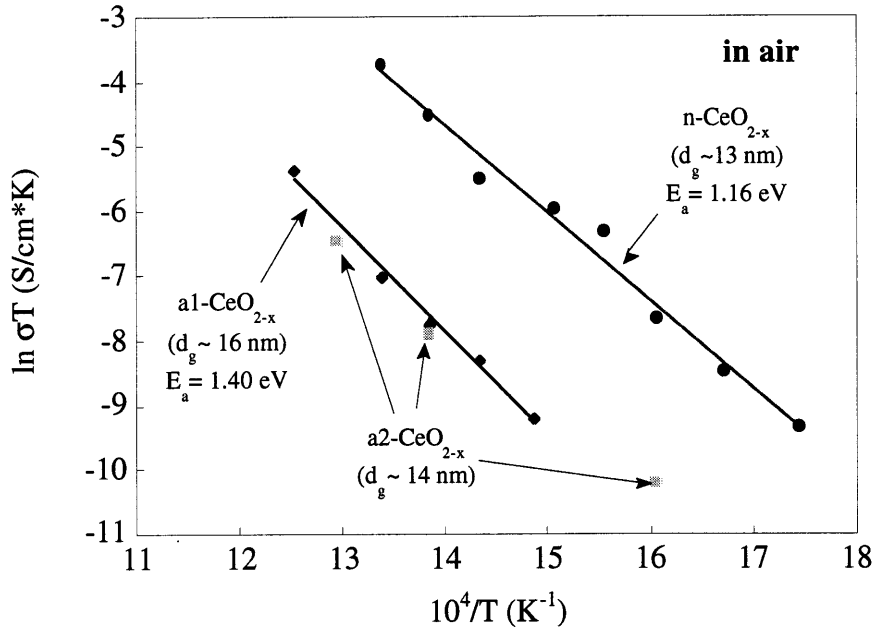
Figure 14: The dependence of conductivity on temperature for the annealed samples, a1-CeO_{2-x}, and a2-CeO_{2-x} as compared with the nanocrystalline sample, n-CeO_{2-x}. The annealed samples are considered to be virtually uncoarsened.

First note that there are only a few data points for the sample, a2-CeO_{2-x}, yet those data points correlate well with the data for the sample a1-CeO_{2-x}. The purpose of the data for a2-CeO_{2-x} is to confirm the evidence that suggests that there are dramatic changes in the conductivity with heat-treatment, even when the heat-treatment causes no change in the grain size of the sample.

Now, consider these dramatic changes in the conductivity more closely. The activation energy for the annealed sample, a1-CeO_{2-x} is slightly larger than that of the as-densified sample, n-CeO_{2-x}, 1.40 eV as compared with 1.16 eV. The difference in conductivity, however is far more striking: the annealed samples exhibit values for the conductivity which are over three orders of magnitude less than that for the as-densified sample. The PO_2 dependence for these samples shows a similarly dramatic drop in conductivity which is depicted in Figure 15.

31
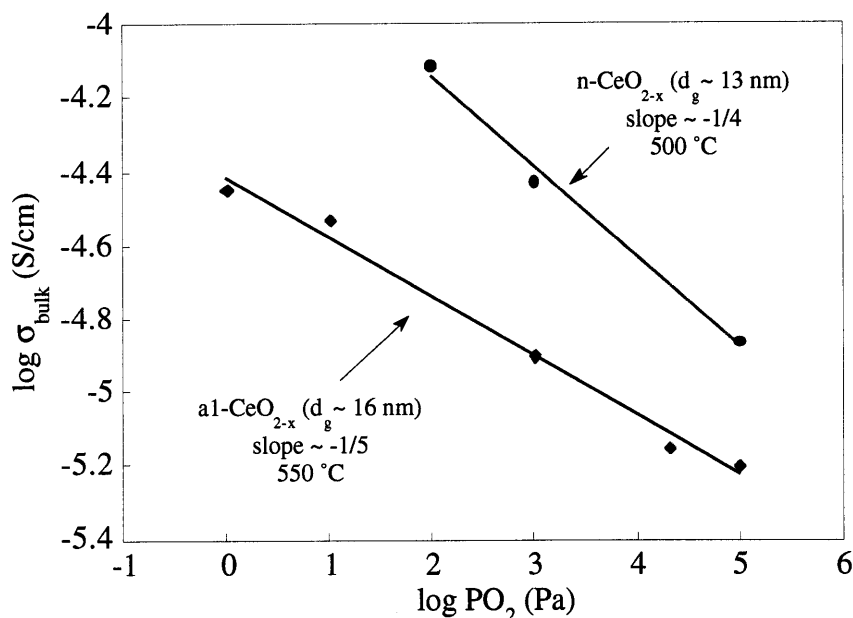
Figure 15: The dependence of the conductivity on the partial pressure of oxygen for the annealed sample, al-CeO$_{2-x}$ as compared with the pure and doped nanocrystalline samples and the coarsened samples. The annealed sample shows a PO$_2$ dependence consistent with reduced behavior, but the conductivity is significantly lower than that for the nanocrystalline samples.

The conductivity is much lower for the annealed sample, al-CeO$_{2-x}$, even though the PO$_2$ dependence was studied at 550 °C in contrast to 500 °C for the as-densified sample, n-CeO$_{2-x}$. However, the oxygen partial pressure dependence of -1/5 for the sample al-CeO$_{2-x}$ is consistent with reduced behavior, since it falls between the -1/4 and -1/6 limits for PO$_2$ dependence based on the doubly ionized oxygen vacancy model. Thus, applying the relations developed from the defect chemistry and described in equations 36 and 37, the activation energy derived from the temperature dependence is low as compared to conventional ceria, and leads to an enthalpy of reduction that is still more than 1.5 eV lower than that for conventional ceria for either the extrinsic or intrinsic reduction models as shown in table 4.

32

Table 4: A Comparison of the volume heat of reduction of the nanocrystalline and annealed samples with the published values

Sample	E_a(eV)	ΔH_R (eV per $V_O^{\bullet\bullet}$)	
		intrinsic, $n = 2[V_O^{\bullet\bullet}]$	extrinsic, $[A'_{Ce}] = 2[V_O^{\bullet\bullet}]$
n-CeO$_{2-x}$	1.16	2.28	1.52
al-CeO$_{2-x}$	1.40	3.00	2.00
Reduced single crystal[14]	1.96	4.67	
Acceptor-doped polycrystals[24]	2.37		3.94

Thus, the annealed sample behaves in a qualitatively similar manner to that of the as densified, nanocrystalline sample in that it exhibits a lower enthalpy of reduction than the conventional ceria, yet the conductivity is three orders of magnitude less than that for the nanocrystalline sample.

To understand why annealing at 700 °C has such a large impact on the conductivity, we return to the model for interfacial reduction. Disorder at the grain boundaries can result in low energy defect sites for which the enthalpy of reduction is lower than within the perfect crystal. For a nanocrystalline material, the high interfacial area leads to domination of the overall enthalpy of reduction by these low energy sites.

The annealed sample's behavior suggests that low energy sites remain, but their density has decreased markedly. Recall that the calculations of Sayle et al.[18] indicate that different crystallographic surfaces exhibit different defect formation energies and that there is a logical correlation between surface behavior and grain boundary behavior. Thus, different grain boundaries should also exhibit different defect formation energies. Polycrystalline material has a spectrum of grain boundary types, so one expects a spectrum of sites of various defect formation energies. The observed enthalpy of reduction is a function of both the number of sites and their formation energies. Since defect formation is activated, the lowest energy sites are the first to form, and thus to be measured. In the nanocrystalline sample, n-CeO$_{2-x}$, there are approximately 10^{17}-10^{18} cm^{-3} such sites on a volume averaged basis[23]. Annealing for even short times at 700 °C appears to decrease the density of these low energy sites by a factor of 10^3. It is logical that the density of sites decreases since low energy sites for formation of defects are essentially high energy sites in the crystal which in the limit of the ideal equilibrium structure, are unfavored. The low energy sites for reduction may be eliminated by atomic rearrangement at

the boundaries. It is logical that the sites for low energy defect formation are those which are very unstable, such as highly disordered boundary sites. It follows, then, that such high energy sites are unfavored and will be rapidly quenched upon annealing for the sample. The slight increase in the enthalpy of reduction is consistent with reduction now taking place at these higher defect formation energy sites.

These results correlate well to the catalytic behavior which both Yao and Yao[5] and Hardacre et al.[7] have observed. Just as the conductivity of nanocrystalline ceria decreases by three orders of magnitude upon annealing at 700 °C, the oxygen storage potential or catalytic activity decreases markedly. Yao and Yao[5] report a 25% drop in the oxygen storage capacity for Pd/CeO_2 and Pt/CeO_2, and a 40% drop for Rh/CeO_2 when the samples are calcined at 800 °C versus 600 °C. Likewise, Hardacre shows that the ratio of the reaction rate to the number of CO_2 molecules produced drops by almost an order of magnitude between 700 K and 900 K. It seems likely, based on this correlation, that the drop in catalytic performance and oxygen storage potential at the surfaces is related to the decrease in conductivity which suggests a decrease in the low energy sites for defect formation at the grain boundaries. This correlation is substantiated by the LEED data of Hardacre et al.[7] which suggests that there is no ordering of their 5.3 monolayer film below 700 K and most of the ordering occurs near 900 K. This ordering is not unlike the proposed atomic relaxation behavior seen in this work.

4.6 The Effect of Coarsening on the Electrical Properties: $c1\text{-}CeO_{2-x}$ and $c2\text{-}CeO_2$

Now, having considered the behavior of the pure, nanocrystalline material, $n\text{-}CeO_{2-x}$, and the affects of heat treatment without coarsening, it is logical to consider how the behavior varies with coarsening. Figure 16 shows a comparison of the temperature dependence of the conductivity for the nanocrystalline sample, $n\text{-}CeO_{2-x}$, the annealed sample $a1\text{-}CeO_{2-x}$ and the coarse samples, $c1\text{-}CeO_{2-x}$, and $c2\text{-}CeO_2$. Recall that the samples were held at temperature until no variations in the conductivity were seen over time scales of at least several hours. In the case of the moderately coarsened sample, $c1\text{-}CeO_{2-x}$, that means that the sample was held at each temperature below 525 °C for at least 19 hours. The values for the even temperatures (350 °C, 400 °C, etc.) were obtained as the sample was heated, and the intermediate values (475 °C, 425 °C etc.) were obtained during the cooling portion of the temperature study. Thus, the kinetically limited, non-equilibrium behavior observed for this sample is real, and not an artifact of the measurements.
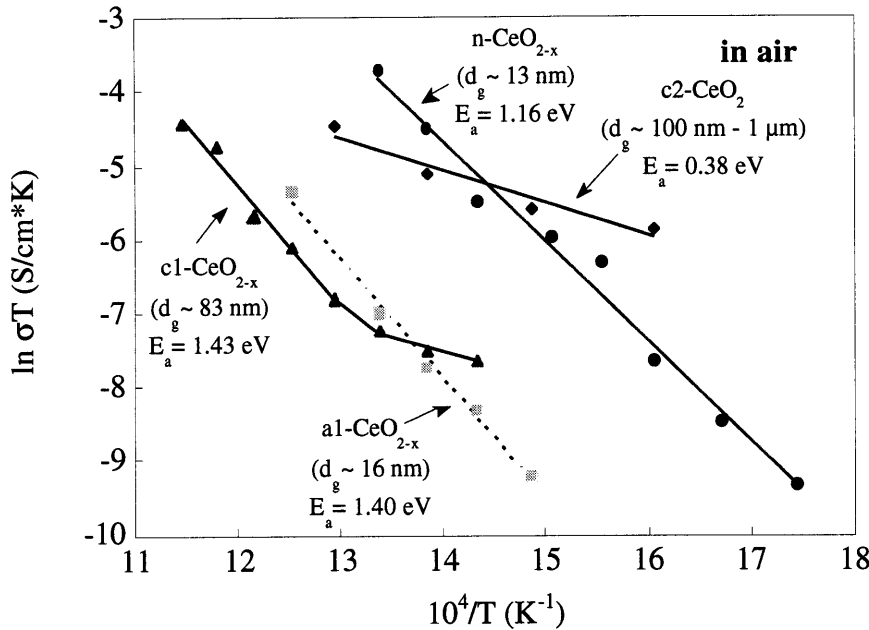
Figure 16: The dependence of conductivity on temperature for the samples n-CeO_{2-x}, $a1$-CeO_{2-x}, $c1$-CeO_{2-x}, and $c2$-CeO_2 demonstrating the effect of coarsening on the conductivity and activation energy. The nanocrystalline ceria is reduced in a region where the coarsest material is not. Likewise, the intermediate grain-size material shows the transition from non-reduced, to reduced behavior.

The coarsest sample, $c2$-CeO_2 shows an activation energy of 0.38 eV which is consistent with the electron hopping energy for ceria[15]. This suggests that the sample is behaving extrinsically under this atmosphere and these temperatures which means that it is kinetically limited and not able to achieve the equilibrium defect concentration with respect to the atmosphere and temperature under these conditions. Similar behavior has been observed by Tuller and Nowick[14] for single crystals of ceria. The relatively high conductivity of this sample is believed to be an artifact of heat treatment which quenched in a population of oxygen vacancies formed at high temperature.

The moderately coarsened sample, $c1$-CeO_{2-x}, shows a similar dependence at low temperatures, below 500 °C, with an activation energy of 0.36 eV, however the conductivity is several orders of magnitude lower. This is most likely because the moderately coarsened sample was less kinetically limited due to its smaller grain-size, and thus avoided the artifact of the heat treatment. This suggests that grain boundary diffusion is the dominant transport mechanism since as the density of grain boundaries is decreased, the sample appears to be more kinetically

limited and behaves extrinsically over a wider temperature range under the same atmosphere. At higher temperatures it displays an activation energy and a conductivity which is comparable to that of the annealed sample, $a1$-CeO_{2-x}. To further understand this temperature dependent behavior, one should consider the PO_2 dependent behavior as depicted in Figure 17.
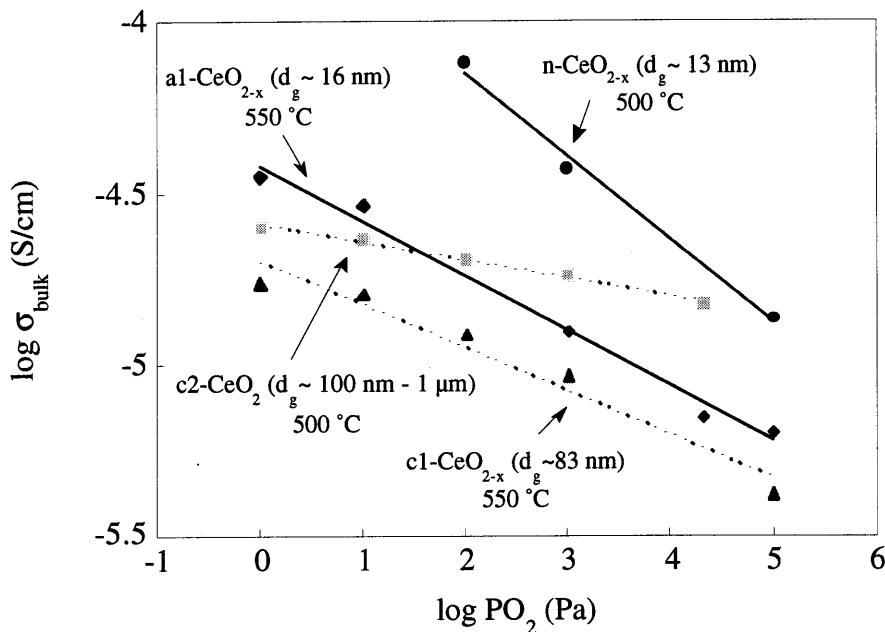

Figure 17: The dependence of the conductivity on oxygen partial pressure for both the nanocrystalline sample, n-CeO_{2-x}, and the coarse samples, $c1$-CeO_{2-x}, and $c2$-CeO_2. The slope for the sample n-CeO_{2-x} is approximately -1/4 which is consistent with extrinsic reduction, but we have not ruled out the intrinsic case in calculating the heat of reduction. The slope for the coarsest sample, $c2$-CeO_2 is approximately -1/20 which is consistent with virtually non-reduced, extrinsic conduction.

The coarsest sample, $c2$-CeO_2, exhibits an extremely weak PO_2 dependence with the slope of the log σ- log PO_2 plot approximately -1/20. The nearly PO_2-independent behavior suggests extrinsic, kinetically limited behavior. The slight PO_2 dependence may result from reduction of the smaller grains in the bimodal distribution which are only a small fraction of the whole and therefore have a minor effect on the total conductivity. The extrinsic behavior of the sample $c2$-CeO_2 substantiates the temperature dependent results in which the sample exhibits an activation energy of 0.38 eV which is consistent with the electron hopping energy for ceria[15].

The moderately coarsened sample, $c1$-CeO_{2-x}, exhibits a PO_2 dependence of slightly less than -1/6 at 550 °C which suggests that the sample is near the reduced region and is consistent

with the temperature dependence (figure 16). The slope is slightly shallow for reduction, but 550 °C is still near the transition area from extrinsic, fixed stoichiometry, to reduced behavior, as inferred from the temperature dependent results, so it is most likely that the slightly weak PO_2 dependence is a reflection of the proximity of the transition region between the two modes of carrier formation.

The essential point demonstrated by the coarsening appears to be one of kinetics. The fact that the moderately coarsened sample exhibits reduced behavior and only shows kinetically limited, extrinsic behavior at low temperatures suggests that it is not as kinetically limited as the coarsest sample, $c2$-CeO_2, and is able to achieve an equilibrium vacancy concentration at moderate temperatures. It is inferred from this that grain boundary diffusion plays a dominant role in the rate of equilibration of ceria.

At higher temperatures, above 500 °C, the sample, $c1$-CeO_{2-x}, appears to be reduced and has an activation energy of 1.43 eV which is slightly higher than that for the nanocrystalline sample, but is still much lower than that for conventional ceria. The corresponding values for the heat of reduction are tabulated in table 5.

Table 5: The Volume Heat of Reduction for n-CeO_{2-x} and its annealed and coarsened counterparts as compared with conventional ceria

		ΔH_R (eV per $V_O^{\bullet\bullet}$)	
Sample	E_a(eV)	intrinsic, $n = 2[V_O^{\bullet\bullet}]$	extrinsic, $[A'_{Ce}] = 2[V_O^{\bullet\bullet}]$
n-CeO_{2-x}	1.16	2.28	1.52
$a1$-CeO_{2-x}	1.40	3.00	2.00
$c1$-CeO_{2-x}	1.43	3.06	2.06
$c2$- CeO_2	0.38		
Reduced single crystal[14]	1.96	4.67	
Acceptor-doped polycrystals[24]	2.37		3.94

Finally, the conductivity of the moderately coarsened sample, $c1$-CeO_{2-x}, is three orders of magnitude lower than that for n-CeO_{2-x} and is very similar to that for the annealed, but uncoarsened sample $a1$-CeO_{2-x}. There is not a three order of magnitude drop in the specific area between the sample n-CeO_{2-x} and $c1$-CeO_{2-x}.

The data regarding the as-densified sample, n-CeO_{2-x}, suggests that at the nanocrystalline size-scale there are unique properties: enhanced electronic conductivity, reduced behavior in regimes where extrinsic behavior is observed, and a lower enthalpy of reduction that

conventional ceria. However, the conductivity does not scale simply with specific surface area. This is shown by figure 18 where the specific surface area was determined using equation 32.
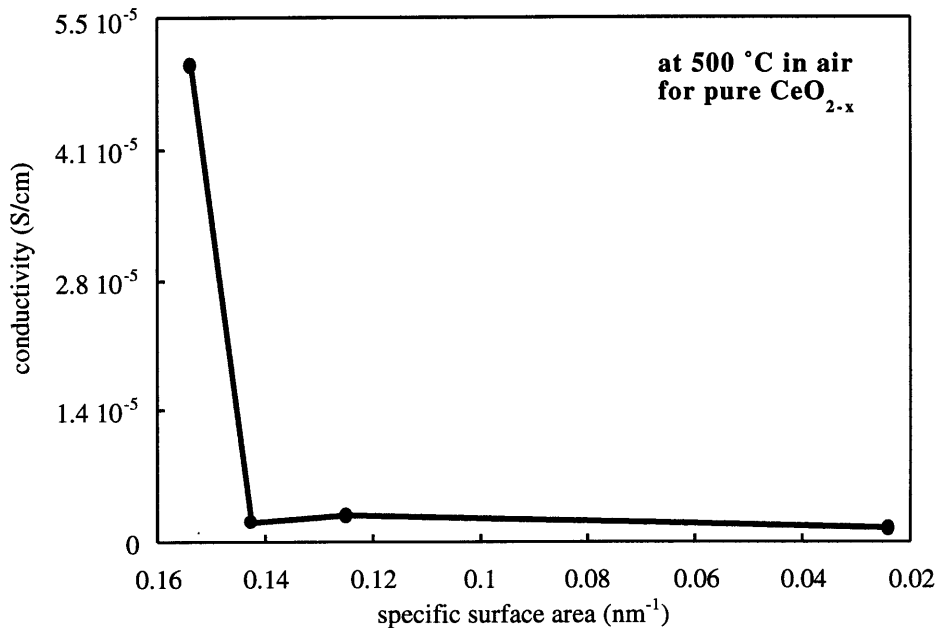

Figure 18: The dependence of the conductivity on specific surface area for pure cerium oxide at 500 °C in air. All of these samples show a similar dependence on the oxygen partial pressure.

If the defect density at the boundaries were constant, the conductivity would scale linearly with the specific surface area. From the data in figure 18, it is clear that the density of defects is not constant. Instead, the variation in the conductivity as a function of grain size is dominated by another phenomenon which is likely the atomic relaxation at the interfaces that quenches the lowest energy sites for reduction.

Both of the nanocrystalline samples, n-CeO_{2-x}, and n-$Ce_{0.9823}Gd_{0.0177}O_{2-x}$, were annealed for several days at 500 °C during electrical measurements, and showed completely reproducible behavior with no variation in the observed conductivity or activation energy after cycling through both temperature and PO_2. Therefore, it appears that the atomistic relaxation to which we attribute the change in defect energies occurs rapidly in the 700 °C temperature range.

4.7 The Conductivity of Lightly Doped Nanocrystalline Cerium Oxide

Figure 17 shows the dependence of the conductivity on temperature for the nanocrystalline pure sample, $n\text{-}CeO_{2\text{-}x}$, as compared with the lightly doped, nanocrystalline sample, $n\text{-}Ce_{0.9823}Gd_{0.0177}O_{2\text{-}x}$.
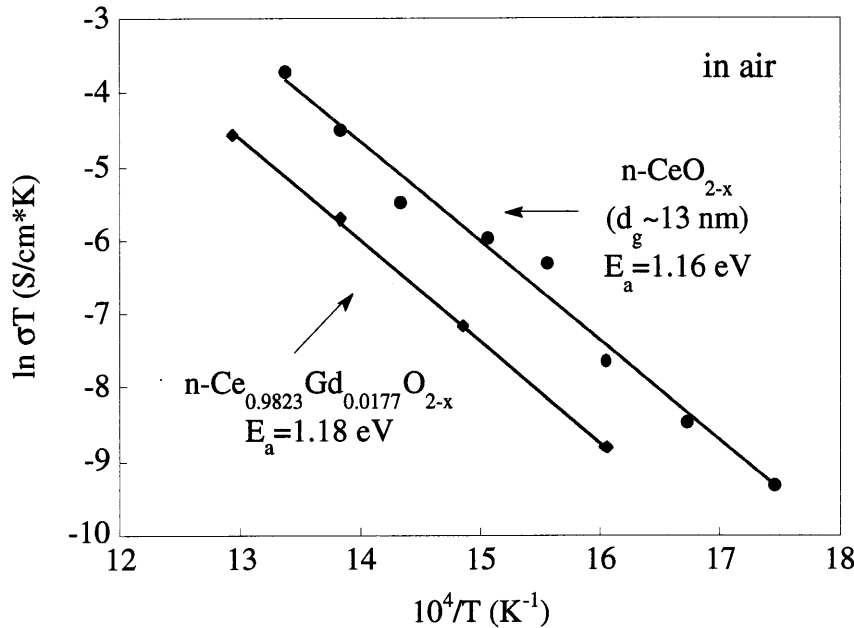

Figure 19: The dependence of conductivity on temperature for the pure nanocrystalline and coarsened samples as compared with the lightly doped sample, $n\text{-}Ce_{0.9823}Gd_{0.0177}O_{2\text{-}x}$, which is also nanocrystalline with a grain size equivalent to that of $n\text{-}CeO_{2\text{-}x}$. Note that the activation energy for the doped sample is equivalent to that of $n\text{-}CeO_{2\text{-}x}$ and that the conductivity is approximately an order of magnitude lower than that for $n\text{-}CeO_{2\text{-}x}$.

The lightly doped sample exhibits the same temperature dependence as the pure nanocrystalline sample, but the conductivity is approximately an order of magnitude lower. Figure 20 shows the PO_2 dependence for the same samples.
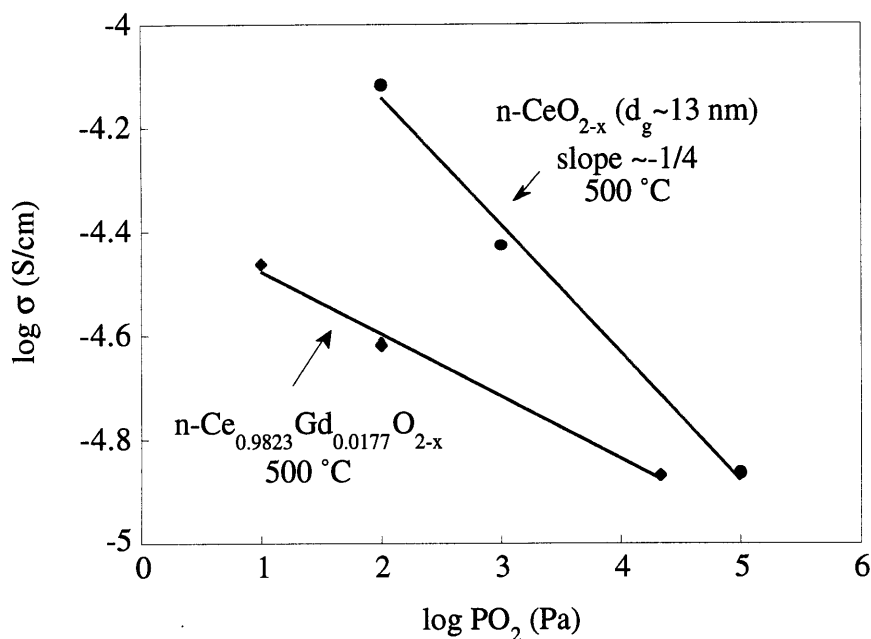
Figure 20: The PO_2 dependence for the conductivity of the nanocrystalline, lightly-doped ceria, n-$Ce_{0.9823}Gd_{0.0177}O_{2-x}$, with the pure nanocrystalline and coarsened ceria samples. The lightly doped sample exhibits PO_2 dependent behavior that suggests electronic conduction as opposed to ionic conduction, in which case it should exhibit PO_2-independent behavior.

The lightly doped, nanocrystalline sample, n-$Ce_{0.9823}Gd_{0.0177}O_{2-x}$, shows a PO_2 dependence of approximately -1/6 which suggests electronic conduction arising from intrinsic reduction. The fact that the activation energy is virtually identical to that of the undoped sample supports the case for reduced, electronic conduction. We attribute this to size-dependent grain-boundary segregation which our group has observed previously[20,21]. Conventional ceria, doped with 1.77% gadolinium should show ionic behavior[22]. However, due to large interfacial area, complete segregation to the grain boundaries occurs leading to exhaustion of the solute within the bulk of the material. This segregation leads to a pinning of oxygen vacancies at the grain boundaries, so that the overall conductivity drops in relation to the doping level. In summary, then, the large interfacial area leads to a depletion of solute and enhanced electronic conduction as compared with the coarsened sample, c1-CeO_{2-x} shown in figures 16 and 17.

It may be possible to create a mixed conductor with doped nanocrystalline material, but it will have to be doped heavily enough to counter the size-segregation effect without altering the nature of the nanocrystalline grain boundaries.

5. Summary and Conclusions

Nanocrystalline cerium oxide, as densified, shows an enthalpy of reduction which is over 2 eV lower than that for the conventional material. It shows reduced behavior in regions where its coarse grained counterparts show non-reduced, extrinsic behavior, and it exhibits enhanced conductivity with respect to moderately-coarsened material.

Annealing the nanocrystalline material without inducing coarsening leads to a slightly higher activation energy, yet the annealed sample still has a heat of reduction which is over 1.5 eV lower than that for conventional ceria. Furthermore, it retains reduced behavior in regions where its coarse-grained counterparts exhibit non-reduced behavior. However, the conductivity is over three orders of magnitude lower than that for the nanocrystalline ceria. We attribute this to atomic relaxation at the grain boundaries which quenches low energy sites for vacancy formation. This effect dominates the conductivity.

Size-segregation effects lead to electronic conductivity in doped cerium oxide at a composition where one would expect to see ionic conductivity in conventional, doped ceria.

Overall, nanocrystalline cerium oxide exhibits unique properties and defect behavior which appear to be a result of disorder at the interfaces leading to a large density of defect sites. Thus the enhanced properties do not appear to scale simply with size.

Bibliography

[1] A. Tschoepe and J. Y. Ying, p. 781 in Nanophase Materials, G. C. Hadjipanayis and R. W. Siegel, eds., Kluwer Academic Publishers, Netherlands, 1994.

[2] W. Liu, and M. Flytzani-Stephanopoulos, submitted to *J. of Catalysis*.

[3] A. Tschoepe, W. Liu, M. Flytzani-Stephanopoulos, and J. Y. Ying, *J. of Catalysis*, **157** 42 (1995).

[4] Su, E. C., and Rothschild, *J. of Catalysis*, **99** 506-510 (1986).

[5] Yao, H. C., and Yao, Y. F. *J. of Catalysis*, **86** 254-265 (1984).

[6] Su, E. C., Montreuil, C. N., and Rothschild, W. G. *Applied Catalysis*, **17** 75-86 (1985).

[7] Hardacre, C., Ormerod, R. M., and Lambert, R. M. *J. Phys. Chem.*, **98** 10901-10905 (1994).

[8] Steele, B. C. H. "State of the Art SOFC Ceramic Materials", in Proceedings of the First European SOFC Forum, 3-7 Oct. 1994, Ulf Bassel, ed., pp. 375-397.

[9] Steele, B. C. H. *Mat. Sci. and Eng.*, **B13** 79-87 (1992).

[10] Kudo, T. and Obayashi, H. *J. Electrochem. Soc.*, **122** 142-147.

[11] Cullity, B.D. Elements of X-Ray Diffraction, 2nd ed. Reading, Massachusetts: Addison-Wesley Publishing Company, inc., 1978.

[12] Macdonald, J.Ross. Impedance Spectroscopy Emphasizing Solid Materials and Systems. New York: John Wiley and Sons, 1987.

[13] Bauerle, J. E., *J. Phys. Chem. Solids*, **30** 2657-2670, 1969.

[14] Tuller, H.L. and Nowick, A.S., *Journal of the Electrochemical Society*, (126) 2, 1979, pp. 209-217.

[15] Tuller, H.L., and Nowick, A.S. *Journal of the Pysics and Chemistry of Solids*, (38), 1977, pp. 859-867.

[16] Blumenthal, R.N. and Hofmaier, R.L. *Journal of the Electrochemical Society*, (121), 1974, pp. 126-131.

[17] Blumenthal, R.N., Lee, P.W., and Panlener, R.J. *Journal of the Electrochemical Society*, (118), 1971, pp. 123-179.

[18] Sayle, T. X. T., Parker, S. C., and Catlow, C. R. A., *Surface Sci.* **316** 329-336 (1994).

[19] Underwood, E. E. Qualitative Sterology, Addison-Wesley, Reading, Mass, 1970.

[20] Terwilliger, C. D., and Chiang, Y. -M., *Acta Metall. Mater.*, **43** 319 (1995).

[21] Chiang, Y. -M., Lavik, E. B., and Blom, D. A., to appear in Nanostructured Materials, vol. 9, 1997.

[22] Aoki, M., Chiang, Y. -M., Kosacki, I., Lee, L. J. -R., Tuller, H., and Liu, Y. *J. Am. Ceram. Soc.*, **79** 1169 (1996).

[23] Chiang, Y. -M., Lavik, E. B., Kosacki, I., Tuller, H. L., and Ying, J. Y. *Appl. Phys. Lett.*, **69** 185 (1996).

[24] Tuller, H. L., and Nowick, A. S. *J. Electrochem. Soc.*, **122** 255 (1975).

Appendix

My Thesis, by Erin Lavik

Introduction

Now here's my work of some import
Which I record 'fore I abort
My travels in this field of stuff
Which makes me say "Enough! Enough!"

Experimental

Now after pouring all the sludge
Into a beaker don't begrudge
Some ice or else use other means
To cool the mixture, else the screams
Will spew forth from your lab-mates scared
By the stuff that fill the air
And then explode with much ado
And coat the labtop, walls, and you.

Discussion

Now here's the data which is true
Although this line seems somehow skewed,
But it is plotted with great care
So moving on, let's leave that there.

Conclusions

Now you have read the record here
Of stuff that's clear and stuff that's queer
And I have told you what I think,
So I'll put down my pen and ink,
And smile and laugh and dance and sing
And savor what is left of spring.